Computational Materials Science 180 (2020) 109723

Contents lists available at ScienceDirect

Computational Materials Science

journal homepage: www.elsevier.com/locate/commatsci

A comparison study between the Lennard-Jones and DRIP potentials for friction of graphene layers

Huyan Li, Woo Kyun Kim*

Department of Mechanical and Materials Engineering, University of Cincinnati, Cincinnati, OH 45221, USA

ARTICLE INFO

Keywords:
Molecular Dynamics
Graphene
Friction

ABSTRACT

Graphene is a promising solid lubricant, in particular for small-length scale devices such as nano/micro-electro-mechanical systems. Atomistic simulations such as molecular dynamics is a popular tool to study the frictional behaviors of graphene layers and it is of critical importance to accurately describe the interlayer interactions in order to give a reliable prediction on the friction of graphene. In this study, the interlayer interactions between graphene layers are examined by using two interatomic potentials, Lennard-Jones (LJ) potential and dihedral-angle-corrected registry-dependent interlayer (DRIP) potential, in the molecular dynamics simulations of friction sliding of multilayer graphene structures. While both potentials have the identical attractive interactions, DRIP models the repulsive interaction by registry-dependent modifiers considering transverse distance and dihedral angle. The sliding simulations mimic the atomic force microscope experiment and are carried out in the zigzag (ZZ) and armchair (AC) directions. The simulation results reveal that the friction forces of the DRIP models are about one order of magnitude larger than those of the LJ models in both sliding directions. It turns out that the modification of the repulsive term in DRIP introduces additional energy corrugations which increase the friction force. Moreover, it is found that the sliding direction is another important factor on friction force of graphene layers so that in both LJ and DRIP models the friction force in the AC sliding direction is about two to three times larger than that of the ZZ sliding.

1. Introduction

Tribological behaviors play an important role in the performance of micro- and nano-scale systems such as micro-electro-mechanical-systems (MEMS), especially those devices in contacting motion, due to the small surface-to-volume ratio and very tight tolerance [1,2]. Graphene is an ideal solid lubricant which can be used to reduce friction and wear of such small-length scale devices thanks to its geometric advantage as an atomically thin 2-D material, low surface energy, and superior resistance to wear in various environments [3–5]. Thus, many research efforts have focused on studying the effects of various factors such as anisotropy, humidity, roughness, normal force, number of layers, etc. on tribological properties of graphene layers via both experimental [6–10] and theoretical/simulation methods [11–17].

Atomistic computer simulations have been widely used in the scrutiny of material behaviors and properties, especially on small length scales, and the interatomic potential which dictates the interaction between atoms is of critical importance in the atomistic simulations. In particular, the accurate modeling of the interlayer interactions between graphene layers is a key factor to the reliability of the friction simulation of graphene systems. One of the most widely used interlayer potentials for graphene is the Lennard-Jones (LJ) potential, which describes the overall binding characteristics between graphene layers (i.e. van-der-Waals interaction) and predicts the equilibrium layer spacing and the c-axis elastic modulus of graphite close to the experimental values [18]. Thus, most theoretical and simulation studies about the tribological properties of graphene have also used the LJ potential [11–13,16,17,19,20]. For example, using the LJ potential Ye et al. [11] found that the number of layers has significant effects on friction of graphene and Li et al. [16] studied the mechanism of transient frictional strengthening on graphene. However, the LJ potential depends only on the interatomic distances between atom pairs so that it fails to describe the energy variation during the sliding and rotational displacements from the equilibrium configuration [21,18]. To correct this drawback, Kolmogorov and Crespi [22] developed a registry-dependent interlayer potential (KC) for graphitic structures by modifying the repulsive interactions to include the overlapping π orbitals of adjacent layers. This modification makes the energy variation due to the transverse displacement accurate. However, it was recently found that the KC potential cannot predict the correct force in the out-of-layer direction

* Corresponding author.
E-mail addresses: li2h9@mail.uc.edu (H. Li), kimwu@ucmail.uc.edu (W.K. Kim).

https://doi.org/10.1016/j.commatsci.2020.109723
Received 30 December 2019; Received in revised form 16 March 2020; Accepted 1 April 2020

when one layer is rotated relative to the other layer [18]. Wen et al.[18] provided a correction to this problem by incorporating dihedral angle dependent terms (See Section 2.2). Their potential is called the dihedral-angle-corrected registry-dependent interlayer potential (DRIP).

In this research, we used the molecular dynamics methodology to study the friction property of graphene layers using the LJ and DRIP potentials. Our friction model consists of the defect-free graphene layers in the AB stacking and the simulation mimics the atomic force microscope (AFM) experiment. The simulation results revealed that the friction forces of the DRIP models are about one order of magnitude larger than those of the LJ models. This article is structured as follows. In Section 2, we explain the simulation model and the two interlayer potentials (LJ and DRIP). The simulation results are presented in Section 3, where some primary differences between the two potentials and the friction force results from the sliding simulation are discussed. Finally, Section 4 provides a summary and conclusions.

2. Models and methods

2.1. simulation model

A schematic representation of the simulation model consisting of 4 graphene layers, labeled layer 1 to 4 from bottom to top, is shown in Fig. 1. We considered two models of different orientation whose x axis is aligned with the zigzag (ZZ) or armchair (AC) directions. Note that Fig. 1 shows only the ZZ model. Each layer in the model has dimensions of 200.757Å × 75.409Å in the x and y directions for the ZZ model and 201.092Å × 74.981Å for the AC model. Since the real graphene layers in use have larger sizes (up to meters [23]) than the simulation models, periodic boundary conditions are applied in the x and y directions to create a pseudo-infinite layer and remove the edge effect, which may be exaggerated otherwise. One layer contains 5,952 atoms in the AC model and 5,976 atoms in the ZZ model, respectively, per the periodic domain. The atom positions of the bottom layer (layer 1) are fixed to prevent the rigid body translation whereas the top layer (layer 4) moves like a rigid body during sliding, i.e., the atoms in layer 4 have no relative motion between them. Atoms in the two middle layers (layer 2 and layer 3) can move freely in all the x, y, z directions except for the atoms in one row, colored red in Fig. 1, which are rigidly attached to layer 1 for layer 2 and layer 4 for layer 3. This arrangement is introduced to ensure that sliding occurs only between layers 2 and 3. Hereinafter, layers 1 and 2 are referred to as the bottom substrate and layers 3 and 4 as the top substrate.

The sliding simulation mimics the AFM experiment so that the top substrate represents the graphene layers attached to an AFM tip, which is pulled by a cantilever sliding against the bottom substrate. The deformation of the cantilever was modeled by a linear spring as shown in Fig. 1. The center of mass (COM) of the top layer is attached to one end of the spring and the other end is connected to a slider so that the spring stores a deformation energy of $\frac{1}{2}k[(x_s - x_{\mathrm{COM}})^2 + (y_s - y_{\mathrm{COM}})^2]$, where x_s and y_s are the x and y coordinates of the slider and x_{COM} and y_{COM} are the x and y coordinates of the COM of the top layer. A spring constant of $k = 47.6$N/m was obtained from the stiffness of an AFM cantilever used in an actual experiment [24]. Thus, the spring can impart both the lateral (F_x) and transverse (F_y) forces on the top substrate as

$$F_x = k(x_s - x_{\mathrm{COM}}), \tag{1}$$

$$F_y = k(y_s - y_{\mathrm{COM}}). \tag{2}$$

During the sliding simulation, the slider moves from the initial location of the COM of the top layer and travels a distance of 25Å only in the positive x direction with a constant velocity of 1 m/s. Thus, y_s remains constant at the initial y coordinate of the COM during the sliding simulation and the transverse force F_y prevents substantial fluctuation of the top layer in the y direction. Unlike the friction force in the AFM experiment that is indirectly measured using the deformation of the cantilever, the friction force in our simulation was directly calculated from the interface force between layers 2 and 3, i.e., the sum of the forces of the atoms in the top substrate exerted by the atoms in the bottom substrate.

The interaction of carbon atoms within the same layer was modeled by the adaptive intermolecular reactive empirical bond order (AIREBO) potential [25] while either the LJ potential or the DRIP potential [18] was employed for interlayer interactions. The LJ potential parameters were adopted from Ref. [26]. The temperature of the system remained constant using Langevin thermostat for all free atoms (blue-colored atoms in Fig. 1) [27,28]. We tested two temperatures of 10 K and 300 K. The simulations were carried out using the large-scale atomic/molecular massively parallel simulator (LAMMPS) program [29] and the post-processing visualizations were performed by the open visualization tool (OVITO) software [30].

2.2. Interlayer interactions

The interactions between carbon atoms in different layers are modeled by either the LJ potential or DRIP potential. First, the LJ potential has the following functional form.

$$V_{\mathrm{inter}}^{\mathrm{LJ}} = \sum_{i\in\mathrm{layer\,1}} \sum_{j\in\mathrm{layer\,2}} \phi^{\mathrm{LJ}}(r_{ij}), \tag{3}$$

where r_{ij} is the interatomic distance between atom i and atom j in different layers and

$$\phi^{\mathrm{LJ}}(r) = 4\varepsilon\left[\left(\frac{\sigma}{r}\right)^{12} - \left(\frac{\sigma}{r}\right)^{6}\right], \tag{4}$$

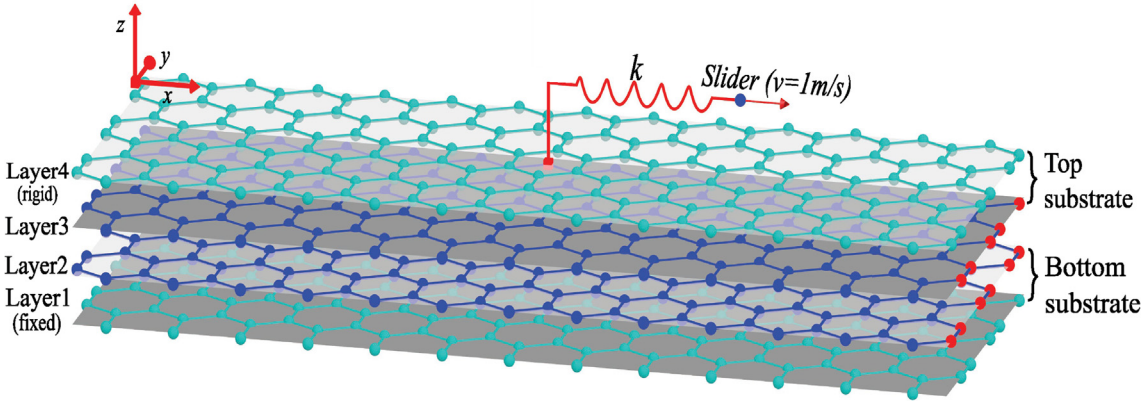

Fig. 1. A schematic representation of the simulation model which consists of 4 graphene layers stacking in the ABAB order. Atoms in blue are free atoms so that they can move freely in all the x, y, z directions.

where ε (=2.168 meV) and σ (=3.36Å) are the LJ parameters [26]. Thus, the interaction due to the LJ potential depends only on the atomic distance.

On the contrary, the DRIP potential incorporates the dependence on the relative configuration of the layers through the transverse distance and dihedral angle as

$$V_{\text{inter}}^{\text{DRIP}} = \frac{1}{2}\sum_{i\in\text{layer 1}}\sum_{j\in\text{layer 2}}(\phi_{ij}^{\text{DRIP}} + \phi_{ji}^{\text{DRIP}}), \tag{5}$$

where

$$\phi_{ij}^{\text{DRIP}} = f_c(x_r)\left[e^{-\lambda(r_{ij}-z_0)}\{C + f(\rho_{ij}) + g(\rho_{ij}, \{a_{ij}^{(m)}\})\} - A\left(\frac{z_0}{r_{ij}}\right)^6\right]. \tag{6}$$

In Eq. (6), $f_c(x_r)$ is a cutoff function of $x_r = r_{ij}/r_{\text{cut}}$, which ensures that the potential and its derivatives are continuous at the cutoff radius r_{cut} = 12Å. While the attractive part of DRIP ($-A(z_0/r_{ij})^6$) is the same as that of the LJ potential (van-der-Waals interaction), it has the Morse-type repulsive part ($e^{-\lambda(r_{ij}-z_0)}$), which is modified by configuration-dependent corrections (transverse distance and dihedral angle) due to overlapping π orbitals between graphene layers.

First, the dependence on the transverse distance is realized through the transverse distance function $f(\rho_{ij})$, where ρ_{ij} is defined as

$$\rho_{ij} = \sqrt{r_{ij}^2 - (\hat{\boldsymbol{n}}_i \cdot \boldsymbol{r}_{ij})^2}, \tag{7}$$

where $\hat{\boldsymbol{n}}_i$ is the unit vector normal to the plane defined by the three nearest neighbors of atom i (k_1, k_2, k_3) and $\boldsymbol{r}_{ij}$ is the displacement vector connecting atoms i and j (See Fig. 2a). The functional relation, plotted in Fig. 2b, is

$$f(\rho) = e^{-y^2}(C_0 + C_2 y^2 + C_4 y^4), \tag{8}$$

where $y = \rho/\delta$ and δ = 0.83679Å. Note that in general $\rho_{ij} \neq \rho_{ji}$ because $\hat{\boldsymbol{n}}_i \neq \hat{\boldsymbol{n}}_j$ so that $\phi_{ij}^{\text{DRIP}} \neq \phi_{ji}^{\text{DRIP}}$.

Next, the dihedral angle dependence is measured through a parameter $\alpha_{ij}^{(m)}$ defined as

$$\alpha_{ij}^{(m)} = \cos\Omega_{k_m ijl_1}\cos\Omega_{k_m ijl_2}\cos\Omega_{k_m ijl_3}\ (m = 1, 2, 3), \tag{9}$$

where Ω_{kijl} is the dihedral angle (torsional angle) defined with atoms k, i, j, l and l_1, l_2, l_3 are the three nearest neighbors of atom j (See Fig. 3a). For example, when a perfect layer 2 where all atoms have three nearest neighbors separated by 120° is in the AA stacking with another perfact layer 1 and is rotated about a fixed atom, we have

$$\alpha_{ij}^{(1)} = \alpha_{ij}^{(2)} = \alpha_{ij}^{(3)} = \cos\theta\cos(\theta + 120°)\cos(\theta - 120°), \tag{10}$$

where θ is the dihedral angle defined with k_m, i, j, l_m (m = 1, 2, 3). Its functional relation is plotted in Fig. 3b. The dihedral angle function g in Eq. (6) is a function of ρ_{ij} and the dihedral angle products $\alpha_{ij}^{(1)}$, $\alpha_{ij}^{(2)}$, $\alpha_{ij}^{(3)}$ as shown in

$$g(\rho, \{\alpha_{ij}^{(m)}\}) = Bf_c(x_\rho)(e^{-\eta\alpha_{ij}^{(1)}} + e^{-\eta\alpha_{ij}^{(2)}} + e^{-\eta\alpha_{ij}^{(3)}}), \tag{11}$$

where $x_\rho = \rho/\rho_{\text{cut}}$ and ρ_{cut} = 1.562Å.

The ten parameters (C_0, C_2, C_4, C, δ, λ, B, η, A, z_0) in the DRIP potential were optimized in comparison with the DFT results based on the exchange-correlation energy of the electrons treated within the generalized gradient approximated (GGA) functional of Perdew, Burke, and Ernzerhof (PBE) [31] and the van-der-Waals correction by the many-body dispersion (MBD) method [32]. The DRIP developers found that the MBD method provides the best overall accuracy for all considered properties. Table 1 shows several key properties computed by the DFT and DRIP potential, extracted from [18]. For full details about the DRIP potential and comparison with the DFT results, see the original reference [18].

3. Results

3.1. Preliminary comparison

Here we show the difference in the interlayer interaction energy between the LJ and DRIP potentials with two rigid perfect layers subjected to the transverse and rotational motion. We first computed the energy per atom by translating the top layer against the bottom layer in the ZZ and AC directions, respectively, from the initial AA stacking position (See Fig. 4a). The interlayer distance is fixed at 3.4 Å. The results are shown in Fig. 4b, where the normalized sliding distance s_r is calculated by s/l_{ZZ} for the ZZ translation and s/l_{AC} for the AC translation and s is the actual sliding distance in each direction. l_{ZZ} and l_{AC} are the unit cell lengths in the ZZ and AC directions, which are $\sqrt{3} \times r_{CC}$ and $3 \times r_{CC}$, respectively, where r_{CC} (=1.3965Å) is the C–C bond length. We used the periodic boundary conditions in the in-plane directions and there are two types of atoms having different energies so the energy per atom shown in Fig. 4b is the averaged value of these two types of atoms. As seen in the figure, the variation in energy is about a factor of 20 larger in DRIP (5.18 meV in ZZ and 5.74 meV in AC) than in LJ (0.256 meV in ZZ and 0.263 meV in AC), which implies that graphene layers should overcome larger energy barriers during sliding than estimated by the LJ potential.

Next, we calculated the energy during rotation of the top rigid layer against the bottom layer in the AA stacking with one atom in each layer fixed (See Fig. 5a). As in the translation, the interlayer distance is fixed at 3.4 Å. Fig. 5b shows the energy of the atom in the bottom layer on the rotation axis. Compared to the translation case, the energy variation in DRIP (5.05 meV) is about two orders of magnitude larger than that in the LJ potential (0.021 meV), which implies that the LJ potential significantly underestimates the rotational resistance of the graphene

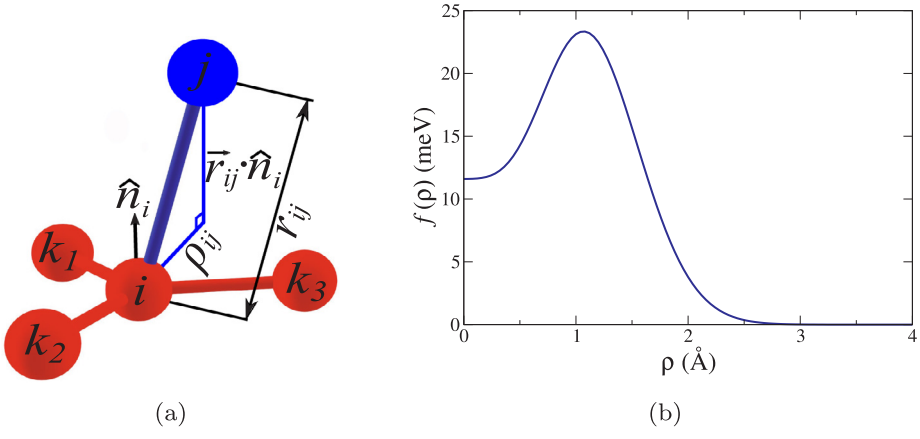

Fig. 2. (a) Definition of the transverse distance ρ_{ij} and (b) the transverse function $f(\rho)$.

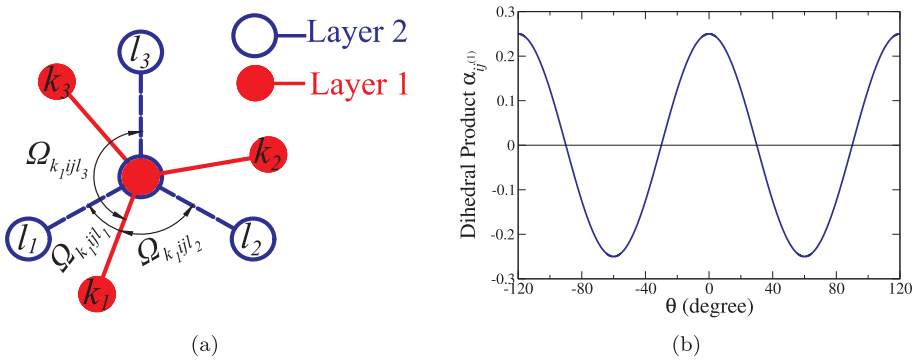

Fig. 3. (a) Definition of the dihedral angles. All atoms are projected into the plane normal to $\boldsymbol{r}_{ij}$. (b) The behavior of dihedral angle product $\alpha_{ij}^{(1)}$.

Table 1
Properties of bilayer graphene are compared by DFT and DRIP. d_{AB}, d_{AA} and $d_{graphite}$ are the equilibrium layer distances in AB, AA stackings and graphite, respectively. E_{AB} and $E_{graphite}$ are the binding energy at equilibrium distance in AB stacking and in graphite. ΔE_{AA-AB} and ΔE_{SP-AB} are energy difference between AA, AB and SP stacking at a layer distance of 3.4 Å. All the results are extracted from [18].

	d_{AB} (Å)	d_{AA} (Å)	$d_{graphite}$ (Å)	E_{AB} (meV/atom)	$E_{graphite}$ (meV/atom)	ΔE_{AA-AB} (meV/atom)	ΔE_{SP-AB} (meV/atom)	C_{33} GPa
PBE + MBD	3.423	3.638	3.398	22.63	48.96	6.17	0.69	31.64
DRIP	3.439	3.612	3.415	23.05	47.38	6.02	0.71	32.00

layers.

3.2. Friction force

Now we present the friction force results calculated from the sliding simulations. All the simulations were repeated three times by assigning different, but statistically equivalent initial velocities. An equilibration simulation was carried out with the slider position fixed before the sliding simulation started. Also, the friction force was calculated by summing the interface forces in the sliding direction between the atoms in the top and bottom substrates as described in Section 2.1.

3.2.1. Sliding in ZZ direction

First, Fig. 6 shows the friction forces as functions of sliding distance when the top substrate is driven in the ZZ direction. As seen in the figures, a typical stick–slip motion was observed in all the samples with both LJ and DRIP. Thus, the top substrate is initially locked with the bottom substrate in the AB stacking corresponding to a local minimum (stick phase), which is characterized by almost linear increase in friction force. As the slider continues to move in the sliding direction and the spring stretches, the lateral force exerted on the top substrate by the spring exceeds a critical limit which the interface between the top and bottom substrates can sustain so that the top substrate starts to slide to a new minimum in the sliding direction (slip phase). During the slip stage, the friction force exhibits an abrupt drop as shown in the figure. The slip event stops as the top substrate becomes pinned at a new minimum and the friction force starts to linearly increase again. This whole process continues to be repeated as the slider moves. In the case of the LJ simulations shown in Fig. 6a, the large (~ 2 nN) and small (~ 0.5 nN) peak forces alternate, which will be explained shortly. Moreover, the figures clearly reveal the difference in the friction force between the LJ and DRIP potentials. The peak forces in the DRIP potential range between 20 and 30 nN, which are about one order of magnitude larger than the LJ peak forces. It is also observed that the friction force of the DRIP simulation always remain positive while the friction force from the LJ simulation fluctuates between the positive and negative values.

In order to better understand the frictional behavior, we constructed the potential energy maps of the LJ and DRIP sliding models, shown in Fig. 7a and Fig. 7b, respectively. In this construction, the top layer is rigidly displaced to a position in the xy plane by a small amount of Δx and Δy in each step. Then, the top layer is allowed to relax only in the z direction with the x and y positions fixed there. During the energy minimization, the atoms in layer 2 and layer 3 are fully relaxed in the

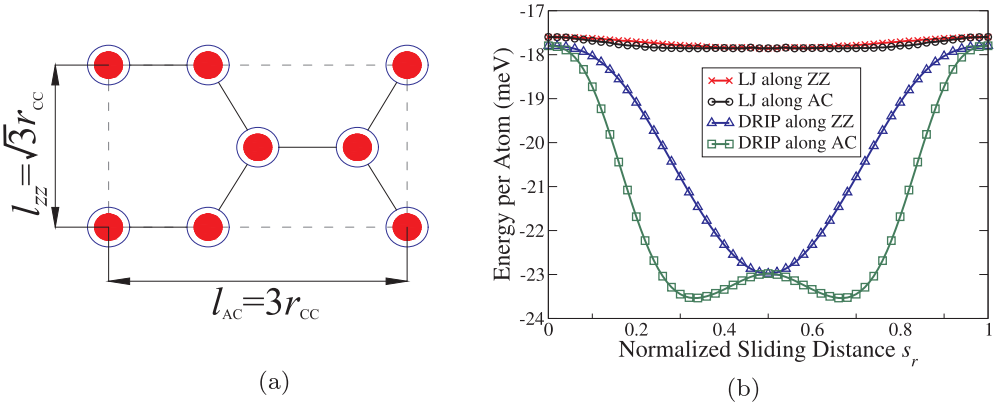

Fig. 4. Difference in energy between LJ and DRIP during translation. (a) Initial configuration of the two perfect layers in the AA stacking; red-filled circles and blue-open circles represent atoms in the bottom and top layers, respectively. (b) Energy per atom as a function of normalized sliding distance in the ZZ and AC directions.

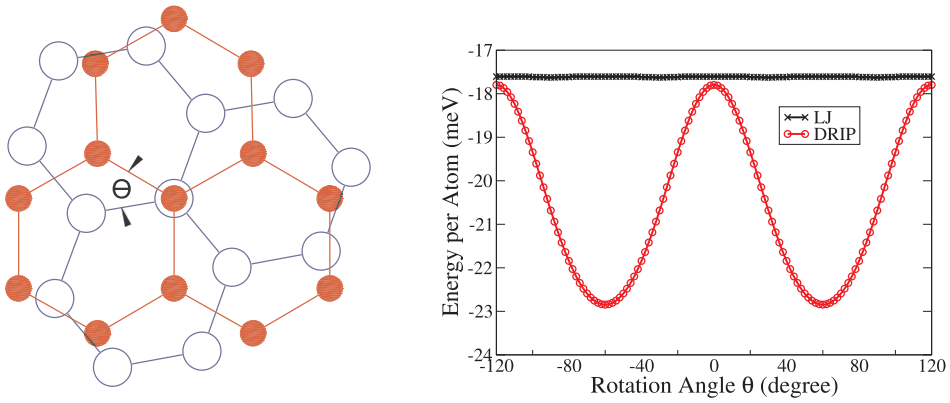

(a) Rotation configuration (b) Rotation energy

Fig. 5. Difference in energy between LJ and DRIP during rotation. (a) A schematic diagram showing the relative configuration during rotation of the top layer against the bottom layer, which is initially in the AA stacking; red-filled circles and blue-open circles represent atoms in the bottom and top layers, respectively. (b) Energy of the atom at the rotation center in the bottom layer as a function of the rotation angle θ defined in (a).

x, y, z directions as in the friction simulation. As seen in Fig. 7a and Fig. 7b, the local minima of both the LJ and DRIP models have a hexagonal arrangement, reflecting the symmetry of graphene layer with two types of different neighboring arrangements, referred to as A and B in the figures. However, the actual scale of the energy in DRIP is much larger than that of the LJ model as seen in Fig. 7c, where the energy is plotted along the path connecting A to B. Moreover, the energy map figures include the trajectory of the top layer in each sample simulation. In the case of the LJ models, the top layer alternates the slip motions from A to B and B to A. Since the top layer starts from a type A minimum and the slider moves only in the x direction, its y position remain fixed as the y position of type A minima (~0Å). As the spring stretches, the slider imparts a lateral force F_x on the top substrate. Since the minimum energy path from A to B is inclined by 30° from the sliding direction, only the component of the lateral force in this direction ($F_x\cos30°$) can be effective to pull the system out of A. When this component exceeds the critical value F_{cr} of the interface, the slip from A to B will occur. Thus, the peak force for A to B slip, $F_{A\to B}$, can be estimated as $F_{cr}/\cos30°$. When the top substrate is pinned at B, there is an extra spring force acting in the positive y direction (F_y) due to the difference in the y position between the slider (y position of A-type minima) and the COM of the top layer (y position of B-type minima). Since only the components of F_x and F_y in the minimum energy path from B to A are effective for the slip from B to A, the slip will occur when $F_x\cos30° + F_y\cos60° \geqslant F_{cr}$. Thus, the peak force for B to A slip, $F_{B\to A}$, is given by $(F_{cr} - F_y\cos60°)/\cos30°$ ($<F_{A\to B}$), which explains why the large and small peak forces alternate in Fig. 6a. The DRIP simulations are more complex. When the first slip event from the initial type A minimum happens, an enormous kinetic energy is released making the top substrate skip several minima before being stabilized into a local minimum. The three sample simulations underwent different initial stages, but eventually all moved to a type B minimum and then only the slip from B to B occurs, i.e., the released kinetic energy is large enough to skip the type A minimum although it is smaller than the first slip value. Thus, the DRIP simulations exhibit the same peak forces after the initial unstable stage (See Fig. 6b).

3.2.2. *Sliding in AC direction*

Next, we discuss the friction force results of the sliding simulation in the AC direction, shown in Fig. 8. As in the ZZ simulations, both the LJ and DRIP models exhibit the stick–slip motions and the friction forces of the DRIP models are one order of magnitude larger than those of the LJ models. Also, like the ZZ sliding, the LJ models exhibit the alternating larger and smaller peak forces, but the larger peak force in the AC sliding is about three times larger than the larger peak force in the ZZ sliding. The same observation was made with the DRIP models, which have two to three times larger peak forces in the AC sliding than the ZZ sliding. Moreover, the three DRIP sample simulations all exhibited the first slip (i.e. the first drop in friction force) at the same slider positions (~ 12.5 Å), but the subsequent events were different.

To understand the difference in friction force between the ZZ and AC sliding, we also created the energy map for the AC model by rotating the energy map of the ZZ model by 90°. The results are shown in Fig. 9, where the four distinguished types of minima are labeled by A, B, A', and B', depending on the arrangement of their neighboring minima. Note that A and A' (also B and B') are the same types of minima, but

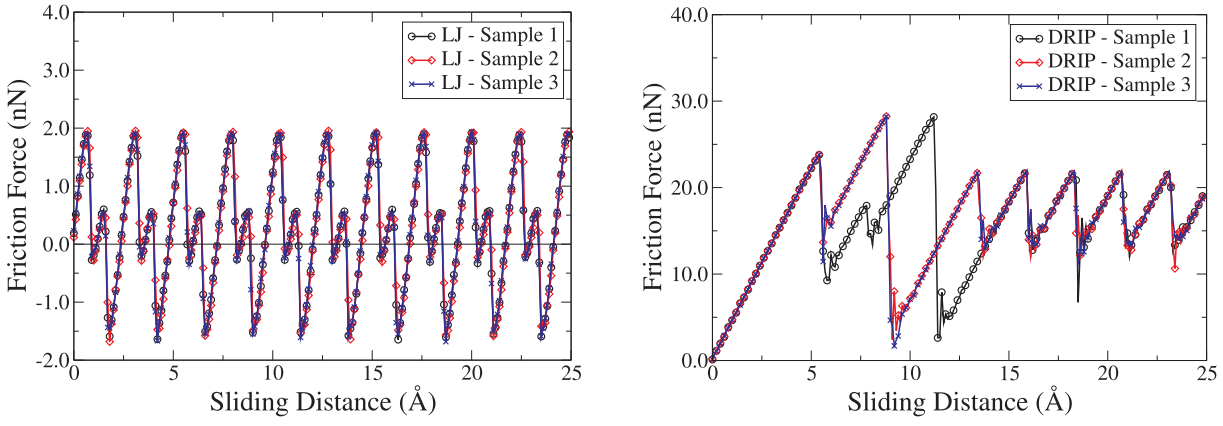

(a) LJ (b) DRIP

Fig. 6. The friction forces of 3 statistically equivalent sample simulations sliding in the ZZ direction, which were calculated using the (a) LJ and (b) DRIP potentials.

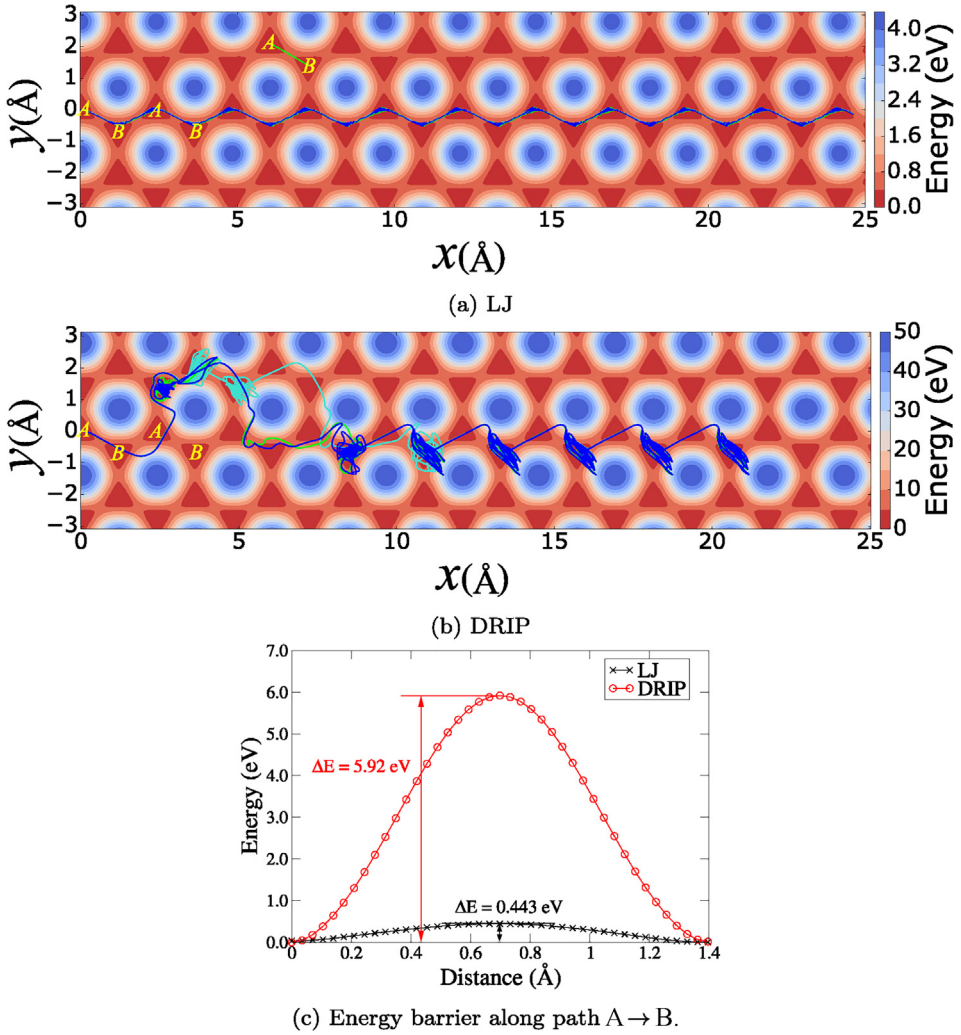

Fig. 7. The potential energy map and the trajectory of the top layer in (a) LJ and (b) DRIP. The local minima are labeled as *A* and *B*, depending on the arrangement of their neighboring minima. Three curves correspond to the trajectories of the three sample simulations; cyan (sample 1), green (sample 2), and blue (sample 3). (c) The energy along the path $A \rightarrow B$ shown in (a).

with different *y* coordinates. As in the ZZ sliding, the slider starts from a type *A* minimum and moves in the sliding direction without changing its *y* coordinate. However, unlike the ZZ sliding, the minimum energy path to the next local minimum *B* is inclined by 60° from the sliding direction so that the required peak force for *A* to *B* slip becomes $F_{cr}/\cos 60°$. As the top substrate climbs up the potential energy hill in the sliding direction, this inclination angle increases, making the required peak force even larger than $F_{cr}/\cos 60°$. Therefore, the AC sliding has larger peak forces than the ZZ sliding, whose peak force is just $F_{cr}/\cos 30°$. In the LJ models, once the slip from *A* is triggered, the top

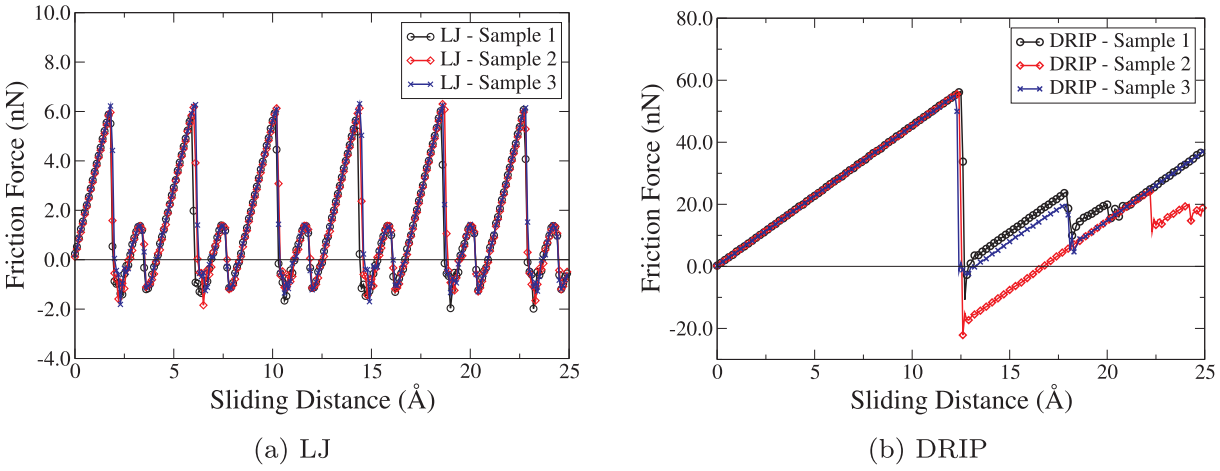

Fig. 8. The friction forces of 3 statistically equivalent sample simulations sliding in the AC direction, which were calculated using the (a) LJ and (b) DRIP potentials.

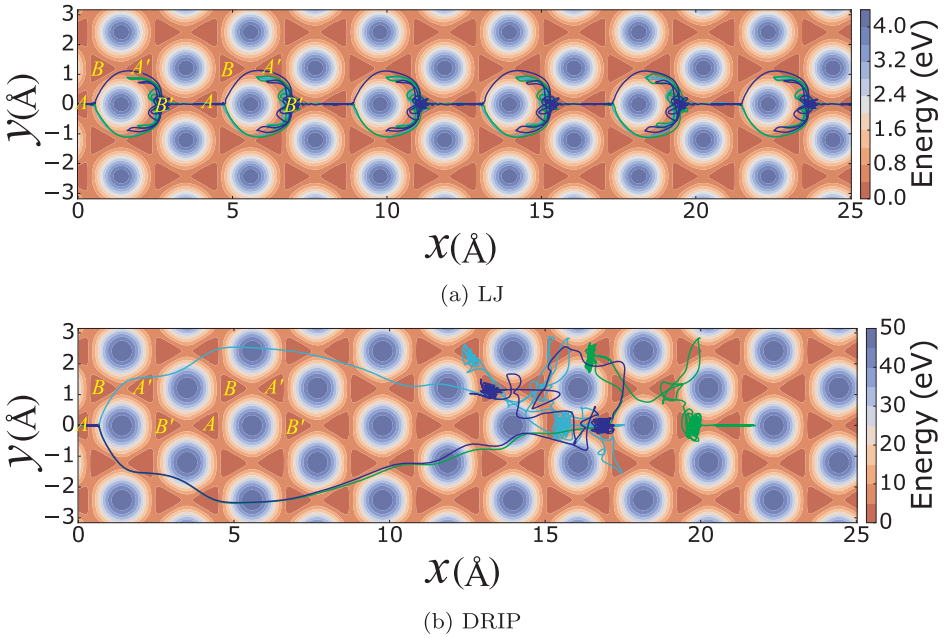

(a) LJ

(b) DRIP

Fig. 9. The potential energy map and the trajectory of the top layer in (a) LJ and (b) DRIP. The local minima are labeled as A, B, A', and B', depending on the arrangement of their neighboring minima. Three curves correspond to the trajectories of the three sample simulations; cyan (sample 1), green (sample 2), and blue (sample 3).

substrate detours around the potential energy hill, passing through the intermediate minima B and A', and eventually becomes pinned at a type B' minimum, which has the same y position as A. The next slip event occurs from B' to A and the smaller peak force shown in Fig. 8a corresponds to this slip event. Then, the same patterns of slip events ($A \rightarrow B \rightarrow A' \rightarrow B'$ and $B' \rightarrow A$) are repeated. In the DRIP models, as shown in Fig. 9b the top substrate traveled longer distances (~ 15 Å) than the LJ models during the first slip due to the larger kinetic energy released after the slip is triggered. Also, each of the three sample simulations moved to a different second minimum, which is off the sliding direction in the y coordinate. Eventually the subsequent slips led the top substrate to the minima having the same y coordinate (A or B') as the initial type A minimum.

3.2.3. Temperature effect

In order to study the effect of temperature on the friction force of graphene layers, simulations were also performed at 300 K. The results are shown in Fig. 10. Compared to the 10 K simulations, there is little difference in the frictional behaviors at 300 K. All the models exhibited the stick-slip behaviors and the friction forces in the AC direction were larger than in the ZZ direction in both the LJ and DRIP potentials. We also calculated the average friction force in each case, shown in Fig. 11. First of all, the average friction forces of the DRIP models are about one order of magnitude larger than those of the LJ models at both 10 K and 300 K. Moreover, the average friction forces of the LJ potential were smaller at 300 K than at 10 K in all the three sample simulations. In particular, the friction force in the AC direction at 300 K was almost twice larger than that in the ZZ direction. However, the friction force in the DRIP potential exhibited little dependence on temperature as seen in Fig. 11b. Also, the friction force of sample 2 in the AC direction (~24 nN) was even larger at 300 K than that at 10 K (~17 nN). We conjecture that this inconsistency might be caused by a smaller number of stick–slip motions observed in the AC sliding of the DRIP potential than in the ZZ direction for the sliding distance of 25 Å.

4. Conclusion

In this study we compared the interlayer interactions modeled by the LJ and DRIP potentials during the molecular dynamics simulations of friction of graphene layers. These two potentials have the similar attractive term based on the van-der-Waals interaction, but DRIP uses the repulsive term modified with transverse distance and dihedral angle dependent parameters. As a preliminary test, we measured the interlayer energy variation by translating or rotating one rigid graphene layer relative to the other. The results showed that the energy variations in DRIP were by a factor of about 200 in rotation and by 20 in translation larger than those in the LJ potential.

Next, we performed the sliding simulations with a model consisting of four defect-free perfect graphene layers in the AB stacking. The simulation mimics the AFM experiment so that the top substrate is pulled by a linear spring as the slider moves at a constant velocity. The simulation was carried out in the ZZ and AC directions at two temperatures of 10 K and 300 K and the friction force was measured by directly considering the interface force between two middle layers where the sliding occurs. All the simulations were repeated three times by assigning different initial velocities in each combination of simulation conditions.

Typical stick-slip motions were observed both in LJ and DRIP models and the LJ models exhibited the alternating larger and smaller peak forces when slips occurred. Moreover, it was found that the friction forces of the DRIP model were about one order of magnitude larger than those of the L-J models in both ZZ and AC sliding directions and at both 10 K and 300 K. To better understand these frictional behaviors, the potential energy maps were computed, where the trajectories of the top layer are also plotted. The energy barrier calculated along the minimum energy path was larger in DRIP than LJ, which explains why the DRIP models have larger friction forces. In the LJ models, the top substrate always exhibited alternating two distinguished slip motions in both ZZ and AC directions. Since the next minimum in the AC direction has a larger inclination angle than in the ZZ direction, a smaller component of the lateral force due to the spring elongation can be used to trigger the slip, making the peak forces in the AC direction larger than those in the ZZ directions. Furthermore, the larger peak force in the DRIP models (i.e. a larger spring energy stored at the onset of slip) released a vast amount of kinetic energy, making the top substrate traveled longer distances than the LJ models and visited different types

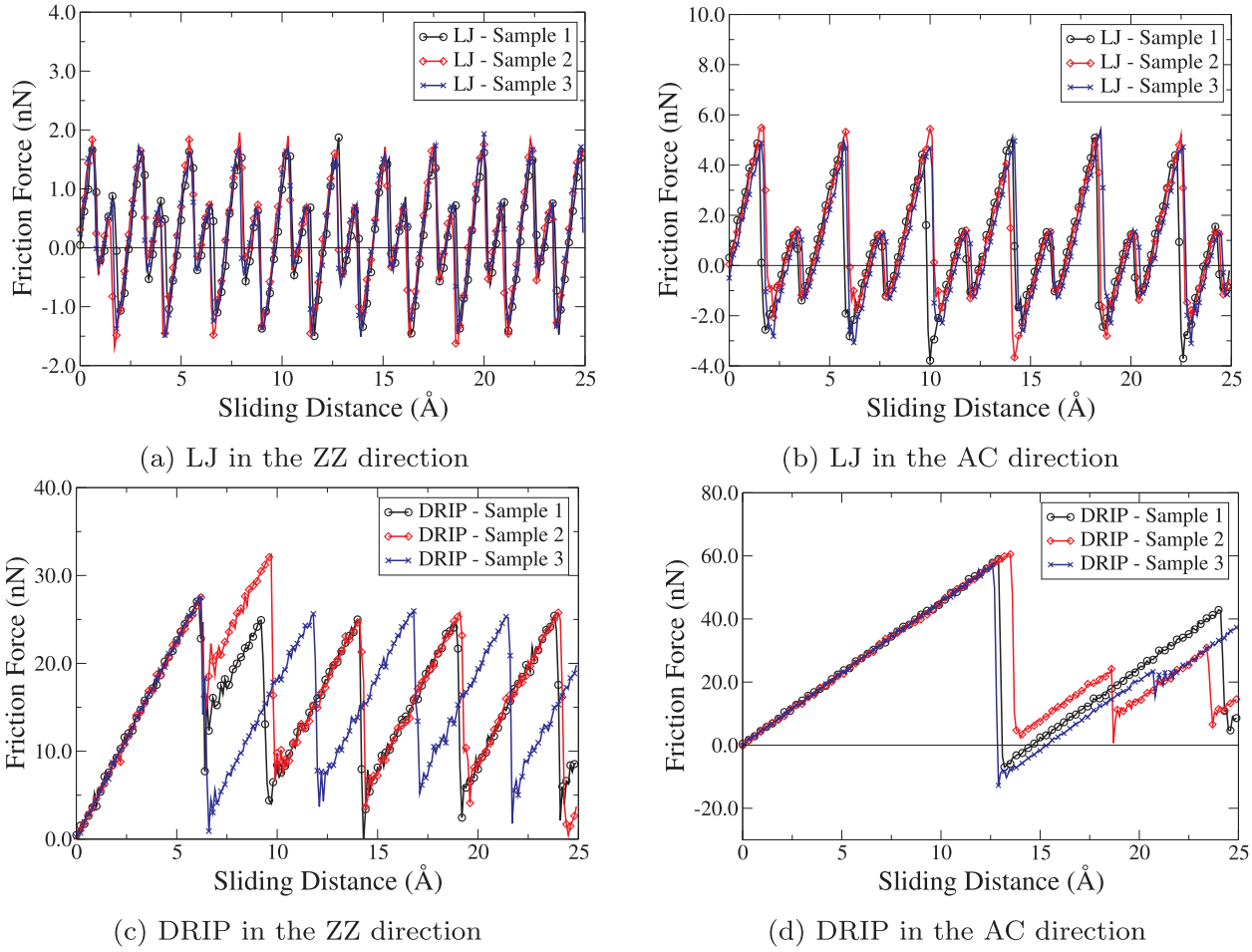

Fig. 10. The friction forces of 3 statistically equivalent samples sliding in the ZZ and AC directions at room temperature (300 K), which were calculated using the LJ potential for (a) and (b) and the DRIP potential for (c) and (d).

of subsequent minima. The DRIP models also had larger friction forces in the AC sliding than the ZZ sliding. Models at a higher temperature of 300 K have similar friction behaviors to those at 10 K. However, overall the average friction force of the LJ potential at 300 K was lower than at 10 K while the DRIP potential exhibited little dependence of the friction force on the temperature.

Since most of the prior studies of graphene friction have used the LJ potential to model the interlayer interactions, we believe that our findings should be taken into account for all future studies in order to obtain more reliable and accurate predictions of the tribological properties of graphene. As a final remark it is noted that the simulation time of DRIP models is about 50 times larger than that of LJ models as the DRIP equations are more complex.

Data availability

The raw/processed data required to reproduce these findings cannot be shared at this time as the data also forms part of an ongoing study.

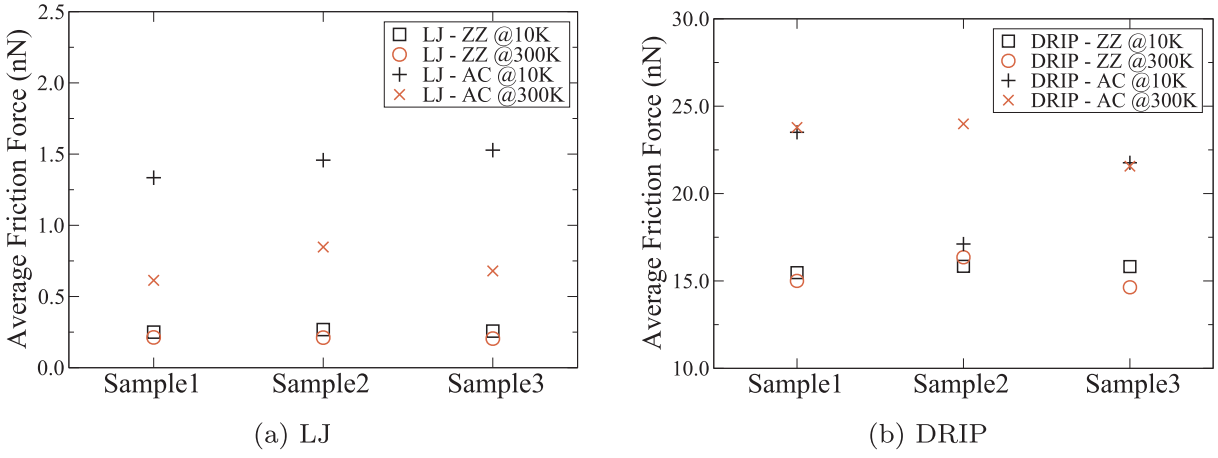

Fig. 11. Average friction force of the LJ and DRIP models in the ZZ and AC sliding directions at temperature of 10 K and 300 K.

CRediT authorship contribution statement

Huyan Li: Data curation, Formal analysis, Investigation, Methodology, Validation, Visualization, Writing - original draft, Writing - review & editing. **Woo Kyun Kim:** Conceptualization, Data curation, Formal analysis, Funding acquisition, Investigation, Methodology, Project administration, Resources, Software, Supervision, Validation, Visualization, Writing - original draft, Writing - review & editing.

Declaration of Competing Interest

The authors declare that they have no known competing financial interests or personal relationships that could have appeared to influence the work reported in this paper.

Acknowledgments

This work was supported in part by the National Science Foundation under Award Number 1662666 and the authors would like to thank E. B. Tadmor at the University of Minnesota for useful discussions.

References

[1] H.-J. Kim, D.-E. Kim, Nano-scale friction: a review, Int. J. Precis. Eng. Manuf. 10 (2) (2009) 141–151.
[2] O. Penkov, H.-J. Kim, H.-J. Kim, D.-E. Kim, Tribology of graphene: a review, Int J. Precis. Eng. Manuf. 15 (3) (2014) 577–585.
[3] S.H. Kim, D.B. Asay, M.T. Dugger, Nanotribology and MEMS, Nano Today 2 (5) (2007) 22–29.
[4] R. Maboudian, W.R. Ashurst, C. Carraro, Tribological challenges in micro-mechanical systems, Tribol. Lett. 12 (2) (2002) 95–100.
[5] D. Berman, A. Erdemir, A.V. Sumant, Graphene: a new emerging lubricant, Mater. Today 17 (1) (2014) 31–42.
[6] T. Filleter, R. Bennewitz, Structural and frictional properties of graphene films on SiC (0001) studied by atomic force microscopy, Phys. Rev. B 81 (15) (2010) 155412.
[7] C. Lee, Q. Li, W. Kalb, X.-Z. Liu, H. Berger, R.W. Carpick, J. Hone, Frictional characteristics of atomically thin sheets, Science 328 (5974) (2010) 76–80.
[8] J.S. Choi, J.-S. Kim, I.-S. Byun, D.H. Lee, M.J. Lee, B.H. Park, C. Lee, D. Yoon, H. Cheong, K.H. Lee, et al., Friction anisotropy–driven domain imaging on exfoliated monolayer graphene, Science 333 (6042) (2011) 607–610.
[9] J. Vilhena, C. Pimentel, P. Pedraz, F. Luo, P.A. Serena, C.M. Pina, E. Gnecco, R. Perez, Atomic-scale sliding friction on graphene in water, ACS Nano 10 (4) (2016) 4288–4293.
[10] Z. Ye, A. Balkanci, A. Martini, M.Z. Baykara, Effect of roughness on the layer-dependent friction of few-layer graphene, Phys. Rev. B 96 (11) (2017) 115401.
[11] Z. Ye, C. Tang, Y. Dong, A. Martini, Role of wrinkle height in friction variation with number of graphene layers, 2012.
[12] Y. Dong, X. Wu, A. Martini, Atomic roughness enhanced friction on hydrogenated graphene, Nanotechnology 24 (37) (2013) 375701.
[13] J.S. Choi, Y.J. Chang, S. Woo, Y.-W. Son, Y. Park, M.J. Lee, I.-S. Byun, J.-S. Kim, C.-G. Choi, A. Bostwick, et al., Correlation between micrometer-scale ripple alignment and atomic-scale crystallographic orientation of monolayer graphene, Sci. Rep. 4 (2014) 7263.
[14] Y. Dong, Effects of substrate roughness and electron-phonon coupling on thickness-dependent friction of graphene, J. Phys. D: Appl. Phys. 47 (5) (2014) 055305.
[15] S. Balakrishna, A.S. de Wijn, R. Bennewitz, Preferential sliding directions on graphite, Phys. Rev. B 89 (24) (2014) 245440.
[16] S. Li, Q. Li, R.W. Carpick, P. Gumbsch, X.Z. Liu, X. Ding, J. Sun, J. Li, The evolving quality of frictional contact with graphene, Nature 539 (7630) (2016) 541.
[17] S.-W. Liu, H.-P. Wang, Q. Xu, T.-B. Ma, G. Yu, C. Zhang, D. Geng, Z. Yu, S. Zhang, W. Wang, et al., Robust microscale superlubricity under high contact pressure enabled by graphene-coated microsphere, Nat. Commun. 8 (2017) 14029.
[18] M. Wen, S. Carr, S. Fang, E. Kaxiras, E.B. Tadmor, Dihedral-angle-corrected registry-dependent interlayer potential for multilayer graphene structures, Phys. Rev. B 98 (23) (2018) 235404.
[19] A. Kavalur, W.K. Kim, Molecular dynamics study on friction of polycrystalline graphene, Comput. Mater. Sci. 137 (2017) 346–361.
[20] H. Li, W.K. Kim, Role of multigrain structure on friction of graphene layers, Comput. Mater. Sci. 165 (2019) 23–33.
[21] K. Zhang, E.B. Tadmor, Energy and moiré patterns in 2D bilayers in translation and rotation: a study using an efficient discrete–continuum interlayer potential, Extreme Mech. Lett. 14 (2017) 16–22.
[22] A.N. Kolmogorov, V.H. Crespi, Registry-dependent interlayer potential for graphitic systems, Phys. Rev. B 71 (23) (2005) 235415.
[23] S. Bae, H. Kim, Y. Lee, X. Xu, J.-S. Park, Y. Zheng, J. Balakrishnan, T. Lei, H.R. Kim, Y.I. Song, et al., Roll-to-roll production of 30-inch graphene films for transparent electrodes, Nature Nanotechnol. 5 (8) (2010) 574.
[24] M. Lantz, S. O'shea, A. Hoole, M. Welland, Lateral stiffness of the tip and tip-sample contact in frictional force microscopy, Appl. Phys. Lett. 70 (8) (1997) 970–972.
[25] S.J. Stuart, A.B. Tutein, J.A. Harrison, A reactive potential for hydrocarbons with intermolecular interactions, J. Chem. Phys. 112 (14) (2000) 6472–6486.
[26] Y. Shibuta, J.A. Elliott, Interaction between two graphene sheets with a turbostratic orientational relationship, Chem. Phys. Lett. 512 (4–6) (2011) 146–150.
[27] T. Schneider, E. Stoll, Molecular-dynamics study of a three-dimensional one-component model for distortive phase transitions, Phys. Rev. B 17 (3) (1978) 1302.
[28] B. Dünweg, W. Paul, Brownian dynamics simulations without Gaussian random numbers, Int. J. Mod. Phys. C 2 (03) (1991) 817–827.
[29] S. Plimpton, Fast parallel algorithms for short-range molecular dynamics, J. Comput. Phys. 117 (1) (1995) 1–19.
[30] A. Stukowski, Visualization and analysis of atomistic simulation data with OVITO–the Open Visualization Tool, Modell. Simul. Mater. Sci. Eng. 18 (1) (2009) 015012.
[31] J.P. Perdew, K. Burke, M. Ernzerhof, Generalized gradient approximation made simple, Phys. Rev. Lett. 77 (1996) 3865–3868, https://doi.org/10.1103/PhysRevLett.77.3865.
[32] A. Tkatchenko, R.A. DiStasio, R. Car, M. Scheffler, Accurate and Efficient Method for Many-Body van der Waals Interactions, Phys. Rev. Lett. 108 (2012) 236402, , https://doi.org/10.1103/PhysRevLett.108.236402.